A Simple Adiabatic Model for Vertical Variation of Halocline Slope in the Beaufort Gyre

Jessica Kenigson

November 25, 2019

1 Introduction

1.1 Forcing, circulation, and freshwater content of the Beaufort Gyre

The Beaufort Gyre is a large wind-driven circulation in the Canada Basin of the Western Arctic Ocean between approximately $120° - 180°$ W and $70° - 85°$ N. Figure 1 shows the bathymetry and spatial pattern of salinity at 200 m in the Beaufort Gyre. The gyre is a persistent feature in the upper ∼300 m of the ocean, driven primarily by the climatological anticyclonic winds associated with the wintertime Beaufort High sea level pressure system. The winds cause Ekman downwelling, which pumps low-salinity surface water into the gyre interior, deepens the halocline, and sets up the resulting anticyclonic circulation. Although the climatological mean winds are anticyclonic, there is considerable seasonal variability; the winds are strongly anticyclonic during the winter and weakest (potentially even cyclonic) during the summer. Nevertheless, the upper-ocean circulation is persistently anticyclonic due to the bowl-shaped deformation of the isopycnals associated with the freshwater storage [9]. The surface waters of the Arctic are relatively fresh due to the excess of precipitation over evaporation in the basin and due to its drainage of numerous large river systems and low-salinity Pacific inflow.

The freshwater content (m) is defined as

$$FWC = \int_D^\eta \frac{S_{ref} - S}{S_{ref}}\, dz \tag{1}$$

where S is measured in practical salinity units, S_{ref} is a reference salinity (typically 34.80), η is the sea surface (m), and D (m) is the depth of the isohaline of the reference salinity [4]. S_{ref} is chosen to be near the mean salinity, and therefore FWC represents the amount of freshwater that would need to be introduced in order to obtain the observed salinity (beginning from S_{ref}). Equation 1 can be integrated over an area of interest to obtain the volumetric fresh water content [4]. The total Arctic freshwater content has been estimated to be 93,000 km^3 over 1980–2000, with 18,500 km^3 being stored in the Beaufort Gyre; over 2000–2010, the Arctic freshwater content increased to 101,000 km^3 and the Beaufort Gyre freshwater content increased to 23,500 km^3 [9]. In addition, the freshwater content of the Beaufort Gyre has been estimated to have increased by 8000 ± 2000 km^3 from 1995–2010

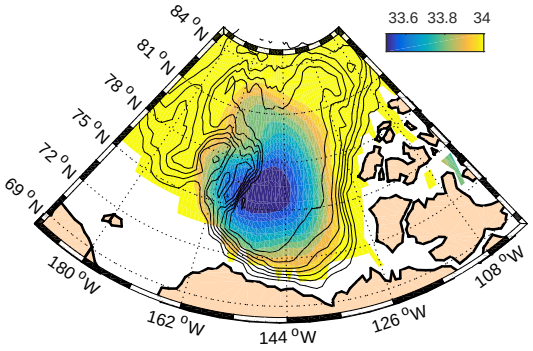

Figure 1: Salinity at 200 m (colormap) from the PHC climatology (winter mean) and bathymetry (black contours). Note the pronounced salinity minimum within the Beaufort Gyre, which is a major freshwater reservoir in the Arctic Ocean.

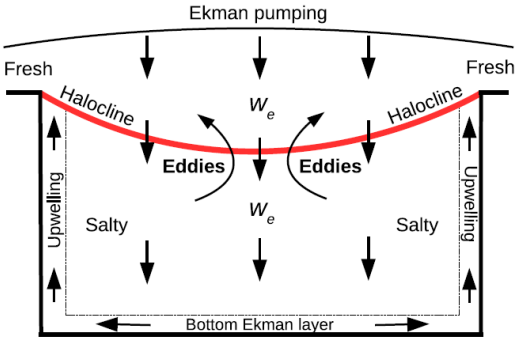

Figure 2: Schematic diagram of the halocline model in [7]. The halocline is represented as an interface that is deepened by Ekman pumping. Mesoscale eddies (baroclinic instability) form along the interface to counteract the deepening. The halocline is modeled to be at a fixed depth at the gyre boundaries. Figure from [7].

due predominantly to the spin-up of the gyre by the increasing trend of the anticyclonic wind stress curl [3].

Wind stress variability over the Beaufort Gyre modulates the storage and release of freshwater, which has implications for freshwater and ice exchanges with the North Atlantic Ocean and the Atlantic Meridional Overturning Circulation (AMOC). It has been proposed that when high sea level pressure and anticyclonic wind anomalies prevail in the Arctic, freshwater accumulates through various mechanisms [9]. River runoff into the Arctic Ocean is enhanced due to shifts in storm tracks. Arctic sea ice also grows during anticyclonic wind regimes due to the cooler temperatures that tend to predominate. Convergence of Ekman transport pumps freshwater into the gyre, which also causes convergence and ridging of sea ice. Finally, export of freshwater through Fram Strait declines, which increases the surface salinity in the Greenland Sea, destabilizes the stratification of the water column and favors deep water formation. As freshwater storage in the Beaufort Gyre is associated with doming of the sea surface, eventually, an anomalous dynamic height gradient between the Beaufort Gyre and the North Atlantic develops, which induces anomalous flow through Fram Strait and the Canadian Arctic Archipelago and sets the stage for a transition to the cyclonic circulation regime. During cyclonic circulation regimes, these processes are reversed.

The halocline in the Canada Basin is subdivided into a "warm halocline" centered around 50 m depth with salinity from ∼30–32 and temperature ∼0 °C, and a "cold halocline" centered around 150 m depth with salinity from ∼32–33 and temperature ∼ −1.5 °C [10]. There is considerable interannual temperature variability and no significant seasonal variability in the warm halocline. The warm halocline is a persistent year-round feature and is sustained by summertime subduction of Chukchi Shelf Waters. The salinity minimum in

the central Beaufort Gyre that is set up by the Ekman pumping prevents strong wintertime mixing that would expose the overlying sea ice to the warm halocline; entrainment of this heat could cause approximately 1 m of sea ice melt [10].

The storage and release of freshwater in the Beaufort Gyre thus has a broad range of implications for the global climate. However, the dynamics of the Beaufort Gyre and the processes that determine the halocline structure are uncertain.

1.2 Beaufort Gyre dynamics and simple model

The Beaufort Gyre is a persistent feature in the Canada Basin [9]. However, until recently the basic dynamical balance of the mean circulation has been unclear. Specifically, what processes oppose the deepening of the halocline due to Ekman pumping, allowing a steady-state circulation to develop?

It has been proposed that mesoscale eddy fluxes are capable of balancing the Ekman pumping in steady state [6]. The bowl-shaped deformation of the isopycnals in the halocline is associated with the buildup of gravitational potential energy, which is a baroclinically unstable configuration that leads to the formation of mesoscale eddies. These eddies act to oppose the steepening of the halocline slope. Experiments with the MITgcm as well as simple scaling arguments [6] suggest that the timescale of adjustment of the gyre to changes in wind forcing (i.e., the time required for the halocline to reach its equilibrium depth) is

$$T \sim \frac{R^2}{K} \tag{2}$$

where R represents the radius of the gyre and K represents the eddy diffusivity. Therefore, for a significant release of freshwater from the Beaufort Gyre to occur, it is necessary for wind forcing anomalies to persist longer than the equilibration timescale, which was estimated to be $\sim$6 years.

The following theory is developed in [7]. In this framework, the halocline is represented as an isopycnal interface that is deepened by Ekman pumping; the deepening of the halocline is opposed by the activity of mesoscale eddies (Figure 2). Assume that

$$\frac{Db}{Dt} = S$$

where b represents buoyancy and S is a source term. Here we model the gyre in cylindrical coordinates. Expanding and taking the Reynolds average of both sides yields

$$\overline{b}_t + \overline{v}\overline{b}_r + \overline{w}\overline{b}_z + \overline{v'b'_r} + \overline{w'b'_z} = \overline{S}. \tag{3}$$

Here v represents a velocity in the r-direction, w represents a velocity in the z-direction, and $\overline{v'b'_r}$ and $\overline{w'b'_z}$ are interpreted as eddy fluxes of buoyancy. It is desirable to re-write the eddy fluxes in Equation 3 as advection of mean buoyancy gradients by eddy velocities v^* and w^*, i.e.,

$$\overline{b}_t + (\overline{v} + v^*)\overline{b}_r + (\overline{w} + w^*)\overline{b}_z = \overline{S}. \tag{4}$$

This condition requires that

$$\overline{v'b'_r} + \overline{w'b'_z} = v^*\overline{b}_r + w^*\overline{b}_z. \tag{5}$$

Using the Transformed Eulerian Mean framework [1], there exists a mean streamfunction $\overline{\Psi}$ such that

$$\overline{v} = -\overline{\Psi}_z, \ \overline{w} = \frac{1}{r}(r\overline{\Psi})_r \tag{6}$$

which satisfies

$$\overline{\Psi} = \frac{\overline{\tau}}{\rho_0 f} \tag{7}$$

where $\tau(r,t)$ represents the (known) azimuthal surface wind forcing of the gyre, ρ_0 is a reference density, and f is the coriolis parameter. In addition, there is an eddy streamfunction Ψ^* with associated eddy velocities

$$v^* = -\Psi^*_z, \ w^* = \frac{1}{r}(r\Psi^*)_r \tag{8}$$

which is given by

$$\Psi^* = -\frac{\overline{w'b'}}{\overline{b}_r} = \frac{\overline{v'b'}}{\overline{b}_z}. \tag{9}$$

This represents the so-called "adiabatic limit" in which eddy fluxes are assumed to be along-isopycnal, i.e., perpendicular to gradients of buoyancy. In this formulation, eddies "re-arrange" existing water masses but do not create "new" water masses (new density classes). This condition can be observed by defining the eddy buoyancy flux as

$$F_b = \begin{pmatrix} \overline{v'b'} \\ 0 \\ \overline{w'b'} \end{pmatrix} \tag{10}$$

and noting that

$$\begin{aligned} F_b \cdot \nabla b &= \overline{v'b'} \cdot \overline{b}_r + \overline{w'b'} \cdot \overline{b}_z \\ &= \overline{b}_r \overline{b}_z \left(\frac{\overline{v'b'}}{\overline{b}_z} + \frac{\overline{w'b'}}{\overline{b}_r} \right) \\ &= 0 \end{aligned}$$

by Equation 9. Using the condition $\nabla \cdot (v^*, 0, w^*) = 0$, which follows from Equation 8, Equation 5 is satisfied. A mesoscale eddy parameterization is needed for the eddy fluxes in Equation 9 and the Gent-McWilliams parameterization [2],

$$\overline{v'b'} = -K\overline{b}_r, \tag{11}$$

is used. Here K ($\mathrm{m}^2\ \mathrm{s}^{-1}$) represents the eddy diffusivity and

$$\Psi^* = Ks \tag{12}$$

by Equation 9, where $s = |\overline{b}_r/\overline{b}_z|$. (For the bowl-shaped deformation of the halocline, it follows that $\overline{b}_r/\overline{b}_z < 0$.)

It is the residual circulation, $\tilde{\Psi} = \overline{\Psi} + \Psi^*$, that drives changes in the halocline depth. Substituting Equations 6 and 8 into Equation 4, it follows that

$$\overline{b}_t + \frac{1}{r}\left(r\tilde{\Psi}\right)_r \overline{b}_z - \tilde{\Psi}_z \overline{b}_r = \overline{S}. \tag{13}$$

In ocean models (e.g., [12]), it is typical for the eddy diffusivity K to be parameterized to be proportional to the isopycnal slope, i.e.,

$$K = ks^{n-1}$$

where k represents the eddy efficiency and n is a small positive integer. This parameterization is used in [7] with $n = 2$. Along with Equations 7 and 12, this implies that

$$\tilde{\Psi} = \frac{\overline{\tau}}{\rho_0 f} + k\left(-\frac{\overline{b}_r}{\overline{b}_z}\right)^2. \tag{14}$$

Equations 13 and 14 are accompanied by the boundary conditions

$$\overline{b}|_{r=R} = b_R(z), \quad \overline{b}_r|_{r=0} = 0, \quad \overline{b}_z|_{z=0,H} = 0, \quad \overline{b}|_{t=0} = b_0(r,z). \tag{15}$$

(From now on, the overbar over Reynolds averaged quantities will be dropped.) Linearizing Equations 13 - 14 about the long-term time mean yields

$$\begin{aligned} b_t + \frac{1}{r}(\tilde{\Psi}r)_r b_{0z} - \tilde{\Psi}_z b_{0r} &= S \\ \tilde{\Psi} &= \frac{\tau}{\rho_0 f} - n\frac{\tau_0}{\rho_0 f}\frac{s}{s_0} \\ \frac{s}{s_0} &= \left(\frac{b_r}{b_{0r}} - \frac{b_z}{b_{0z}}\right). \end{aligned}$$

Here subscripts "0" indicate the basic state and other variables indicate perturbations about the basic state. Defining $h = b/b_{0z}$, where h represents the isopycnal depth perturbation, these equations imply

$$h_t = \frac{1}{r}(nK_0 r h_r)_r + \frac{1}{r}\left(r\frac{-\tau}{\rho_0 f}\right)_r \tag{16}$$

where

$$K_0 = k s_0^{n-1} = k\left(\frac{-\tau_0}{\rho_0 f k}\right)^{(n-1)/n}, \tag{17}$$

and $n = 2$ is, again, a reasonable choice. The boundary conditions for the linearized depth perturbation equation are given by

$$h|_{r=R} = 0, \quad h_r|_{r=0} = 0. \tag{18}$$

Equations 16 - 18 are derived in the appendix of [7]. A gyre adjustment timescale is also derived in [7] and is obtained by decomposing the (nondimensionalized) eddy diffusion operator

$$L := \frac{1}{r}(K_0 r h_r)_r$$

into orthogonal eigenmodes h_i^* and expressing

$$h = \sum_{i=1}^{\infty} a_i(t) h_i^*$$

where $a_i(t)$ is an amplitude function that is exponentially decaying on a timescale T_i. The equilibration timescale of the gyre is set by the slowest timescale

$$T_0 = \frac{1}{n\lambda}\frac{R^2}{K_0(R)}$$

where the eigenvectors h_i and eigenvalues λ are shown in Figure 6 of [7].

2 Extension of the Simple Model

2.1 Rationale for a modified model

The boundary conditions of the existing model assume that the isopycnal interface representing the halocline is at a fixed depth at the boundary of the gyre (see Figure 2). However,

observations suggest that there is considerable seasonal variability in isopycnal outcropping location [10].

The Polar Science Center Hydrographic Climatology (PHC) provides gridded ($1^\circ \times 1^\circ$) means of summer (July, August, September) and winter (March, April, May) temperature and salinity at a sequence of depths between 0 and 5500 m (Figure 3, left and central columns). We use the Thermodynamic Equation of SeaWater 2010 (TEOS-10) equations [5] to estimate the winter and summer climatological density and potential density (Figure 3, right column).

Figure 3 reveals considerable seasonal variability of buoyancy, particularly within the upper $\sim$50 m of the gyre. This variability is predominantly associated with the seasonal variability of salinity rather than temperature, and there is seasonal outcropping of isopycnals (compare the top and bottom rows of Figure 3). Since this variability in the isopycnal outcropping location cannot be captured by the existing model, we modify the model to accommodate it.

Specifically, we consider Equation 16 with the modified boundary conditions

$$h_r|_{r=0,R} = 0 \tag{19}$$

i.e., no flux is permitted through the gyre boundary.

2.2 Solution of linearized equations in an idealized case

We first consider a simplified case of Equation 16 with boundary conditions given by Equation 19 in which K_0 is constant with respect to r and $\tau = 0$. In this case Equation 16 simplifies to

$$h_t = \frac{nK_0}{r}(h_r + rh_{rr}).$$

Suppose that there is a solution of the form

$$h = a(t)b(r).$$

Then

$$a'(t)b(r) = nK_0\left(\frac{1}{r}a(t)b'(r) + a(t)b''(r)\right).$$

Separating variables,

$$\frac{a'(t)}{a(t)} = nK_0\left(\frac{1}{r}\frac{b'(r)}{b(r)} + \frac{b''(r)}{b(r)}\right).$$

Then the LHS implies

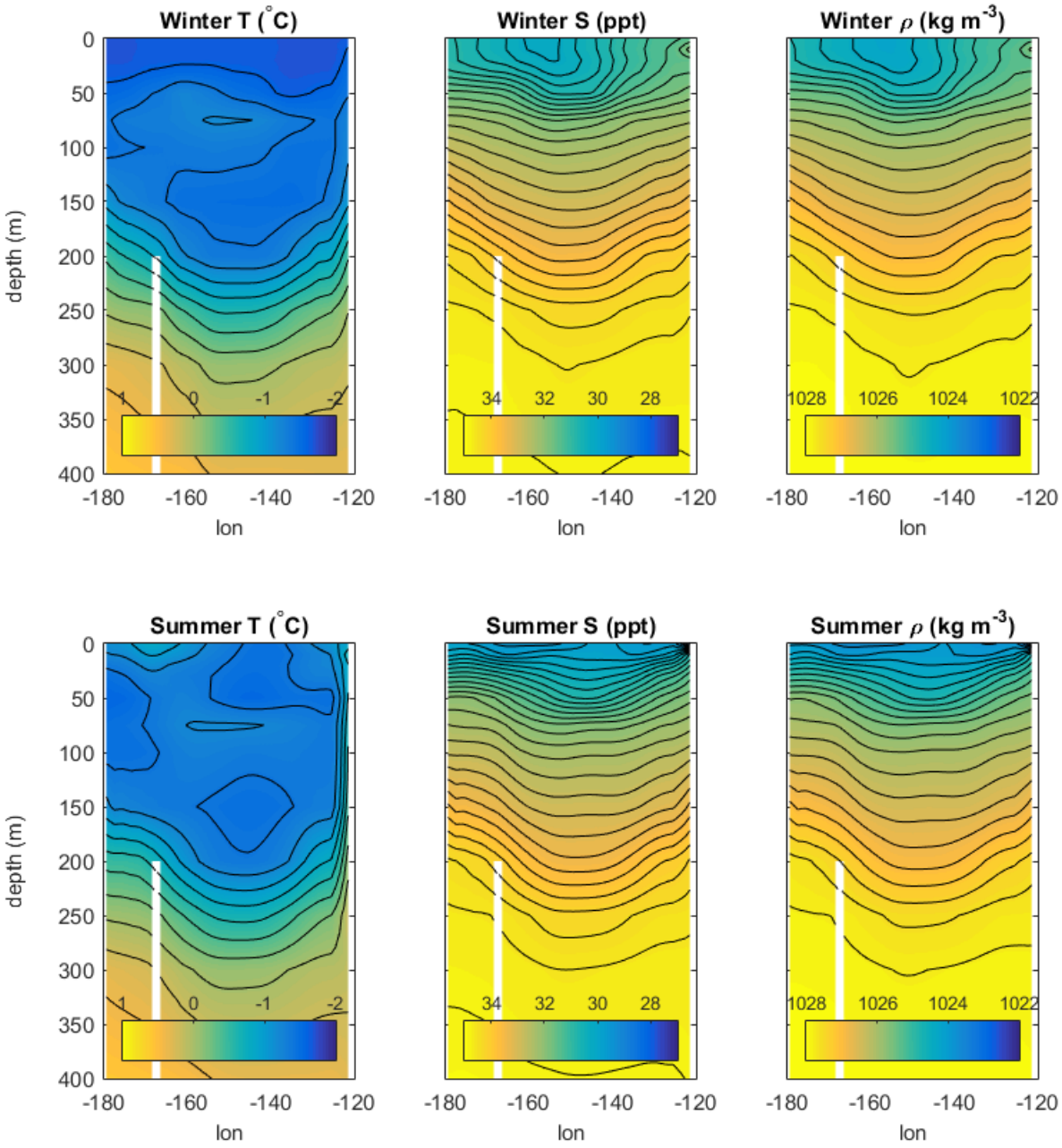

Figure 3: Longitude-depth transect of winter (March, April, May) and summer (June, July, August) mean temperature and salinity from the PHC climatology in the upper 400 m of the Beaufort Gyre at 75.5° N (left and central columns). Potential density is estimated from the TEOS-10 equations using the temperature and salinity profiles (right column).

$$\frac{a'(t)}{a(t)} = -\lambda$$

for some $\lambda \geq 0$, and therefore

$$a(t) = c_0 e^{-\lambda t}$$

for any constant c_0. The RHS implies

$$nK_0 b''(r) + \frac{nK_0}{r} b'(r) + \lambda b(r) = 0$$

or equivalently

$$r^2 b''(r) + r b'(r) + \frac{\lambda}{nK_0} r^2 b(r) = 0.$$

With the substitution

$$c^2 = \frac{\lambda}{nK_0}$$

the equation is seen to have solutions $J_0(cr)$ (Bessel function of the first kind) and $Y_0(cr)$ (Bessel function of the second kind). The general solution to the separable PDE is then

$$h(r,t) = c_0 e^{-\lambda t} \left(c_1 J_0 \left(\sqrt{\frac{\lambda}{nK_0}} r \right) + c_2 Y_0 \left(\sqrt{\frac{\lambda}{nK_0}} r \right) \right)$$

for $\lambda \geq 0$. The values of λ for which nontrivial solutions exist are constrained by the boundary conditions. In the case of the simple halocline model in [7] with boundary conditions given by Equation 19, the condition $h_r|_{r=0} = 0$ requires $c_2 = 0$. The condition $h_r|_{r=R} = 0$ requires

$$\lambda_m = \frac{nK_0}{R^2} \alpha_{1m}^2, \ m = 0, 1, ...$$

where α_{1m} is the m-th zero of the Bessel function J_1. In that case

$$h(r,t) = \sum_{m=0}^{\infty} c_m e^{-\lambda_m t} J_0 \left(\sqrt{\frac{\lambda_m}{nK_0}} r \right).$$

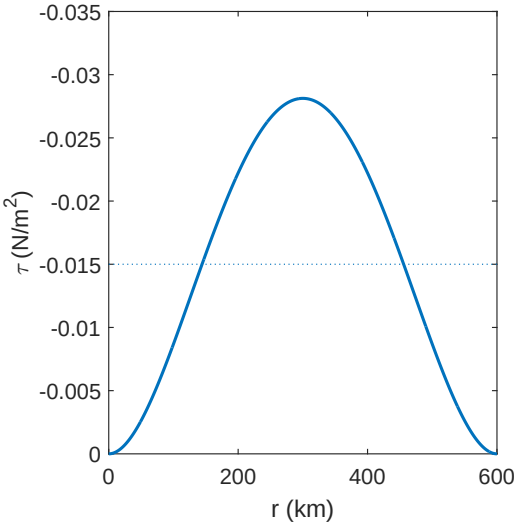

Figure 4: Diagram of the basic state wind forcing given by Equation 20.

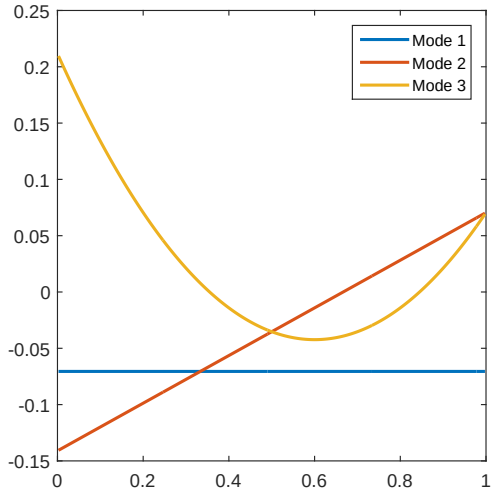

Figure 5: Eigenfunctions of Equation 24 corresponding to the first three eigenvalues $\hat{\lambda} = 0, 3, 8$. (The eigenfunctions are not normalized to be orthonormal.)

2.3 Eigenanalysis of linearized equation in the absence of wind forcing perturbation

In reality, K_0 varies spatially, in balance with the basic state wind forcing τ_0 (Equation 17). Therefore, Equation 16 does not lend itself to a simple analytical solution.

2.3.1 Basic state wind forcing

The wind forcing τ is assumed to be a known function. We assume that it has the form

$$\tau_0(r) = -30\tau_M \left(\frac{r}{R}\left(1 - \frac{r}{R}\right)\right)^2 \tag{20}$$

where τ_M represents the magnitude of the mean value of τ_0 over the gyre. That is,

$$\tau_M = \left| \frac{1}{A} \int_0^{2\pi} \int_0^R \tau_0(r, \theta)\, r\, dr d\theta \right|$$

where $A = \pi R^2$ is the area of the gyre. Here we take $\tau_M = 0.015$ N m^{-2}, which is chosen to facilitate comparison with [7]. Figure 4 shows the basic state wind forcing.

2.3.2 Eigenanalysis

Suppose that $\mathcal{L}[h]$ is a self-adjoint linear operator on a space of real-valued functions $\mathcal{F}$ defined on $[0, R]$ which are integrable with respect to an r-weighted inner product

$$\langle f, g \rangle = \int_0^R r f(r) g(r)\, dr. \tag{21}$$

Then the eigenfunctions of $\mathcal{L}$ form a complete orthonormal basis h_i^* such that for any function h in $\mathcal{F}$,

$$h = \sum_{i=0}^{\infty} c_i(t) h_i^*$$

where $c_i = \langle h, h_i^* \rangle$. We examine the eigenfunctions of the linear operator

$$\mathcal{L}[h] = \frac{1}{r}(K_0(r) r h_r)_r, \quad h_r(0) = 0, \quad h_r(R) = 0. \tag{22}$$

Lemma 2.1 *The linear operator defined by Equation 22 is self-adjoint with respect to the inner product given by Equation 21.*

Proof

$$\begin{aligned}
\langle \mathcal{L}[f], g \rangle &= \int_0^R (K_0 r f_r)_r g\, dr \\
&= \int_0^R (K_0 r f_r g)_r\, dr - \int_0^R (K_0 r g_r) f_r\, dr \\
&= (K_0 r f_r g|_0^R - \int_0^R (K_0 r g_r f)_r\, dr + \int_0^R (K_0 r g_r)_r f\, dr \\
&= (K_0 r g_r f|_0^R + \langle f, \mathcal{L}[g] \rangle \\
&= \langle f, \mathcal{L}[g] \rangle\,.
\end{aligned}$$

Although we cannot solve Equation 16 analytically, as in [7] the solution h can be decomposed into spatially-varying orthogonal modes (eigenvectors) h_i with amplitudes $c_i(t)$ which are exponentially decaying on a timescale T_i (inversely proportional to eigenvalues λ_i). Therefore, we consider the eigenvalue problem

$$\frac{n}{r}\left[r K_0(r) h_r\right]_r = -\lambda h \tag{23}$$

subject to the boundary conditions (Equation 19). It is considerably more convenient to solve the nondimensionalized problem that results from choosing

$$\hat{r} = r/R, \quad \hat{h} = h/R, \quad \hat{K_0} = K_0(r)/K_0(R/2), \quad \hat{T} = (nTK_0(R/2))/R^2.$$

The resulting problem is given by

$$[\hat{r}\hat{K_0}\hat{h}_{\hat{r}}]_{\hat{r}} = -\frac{\hat{r}\hat{h}}{\hat{T}} = -\hat{\lambda}\hat{r}\hat{h} \tag{24}$$

where $\lambda := 1/T$ and $\hat{K_0} = 4\hat{r}(1-\hat{r})$ by Equation 17 and Equation 20. The nondimensionalized boundary conditions become

$$\hat{h}_{\hat{r}}|_{\hat{r}=0,1} = 0. \tag{25}$$

Then the timescale of equilibration of the gyre is given by

$$T_0 = \frac{1}{\lambda_0} = \frac{R^2\hat{T}_0}{nK_0(R/2)} = \frac{R^2}{n\hat{\lambda_0}K_0(R/2)}$$

where the eigenfunctions are assumed to be sorted such that λ_0 is smallest, i.e., T_0 is longest. Thus the equilibration is controlled by the slowest eigenfunction.

We solve Equation 24 numerically. The first three eigenvalues are $\hat{\lambda} = 0, 12, 32$ and the eigenfunctions are shown in Figure 5.

2.4 The nonlinear problem

2.4.1 Steady state solution

In steady state, the residual circulation vanishes, i.e., $\tilde{\Psi} = 0$. It follows from Equation 14 that

$$h(r) = -\int_0^r \left(\frac{-\tau(r')}{\rho_0 f k}\right)^{\frac{1}{2}} dr' + h(0). \tag{26}$$

Assume that the surface wind stress is given by Equation 20. Then Equation 26 implies

$$h(r) = -\left(\frac{30\tau_M}{\rho_0 f k}\right)^{\frac{1}{2}} \left(\frac{r^2}{2R} - \frac{r^3}{3R^2}\right) + h(0). \tag{27}$$

There is no particular reason that $h(r)$, as given by Equation 27, must be positive. Given that

$$-\left(\frac{30\tau_M}{\rho_0 f k}\right)^{\frac{1}{2}} \left(\frac{r^2}{2R} - \frac{r^3}{3R^2}\right) = -\left(\frac{30\tau_M}{\rho_0 f k}\right)^{\frac{1}{2}} \frac{r^2}{R}\left(\frac{1}{2} - \frac{r}{3R}\right) < 0$$

for $0 \leq r \leq R$, the sign of $h(r)$ depends upon the choice of $h(0)$. If $h(0)$ is sufficiently large, then $h(r) > 0$ for all r, i.e., the isopycnal does not "outcrop." There is a relationship between the location at which the steady state solution outcrops and the volume V that is bounded between the isopycnal and the surface. If the isopycnal does not outcrop, then

$$V = 2\pi \int_0^R rh(r)\,dr = -\frac{70\pi C R^3}{60} + h(0)\pi R^2 \tag{28}$$

where

$$C = \left(\frac{30\tau_M}{\rho_0 f k}\right)^{\frac{1}{2}}. \tag{29}$$

Otherwise,

$$V = 2\pi \int_0^{y_0} rh(r)\,dr = -\frac{\pi C y_0^4}{4R} + \frac{2\pi C y_0^5}{15R^2} + \pi y_0^2 h(0) \tag{30}$$

where $r = y_0$ is the outcropping location (i.e., the location at which $h(y_0) = 0$). Substituting $h(0)$ from Equation 27 into Equation 30 (with $h(y_0) = 0$), it follows that

$$\frac{V}{2\pi C} = -\frac{1}{10R^2} y_0^5 + \frac{1}{8R} y_0^4.$$

Let

$$q(y_0) := -\frac{1}{10R^2} y_0^5 + \frac{1}{8R} y_0^4 - \frac{V}{2\pi C}. \tag{31}$$

Suppose that $0 \leq y_0 \leq R$. Then

$$q'(y_0) = -\frac{1}{2R^2} y_0^4 + \frac{1}{2R} y_0^3 = \frac{y_0^3}{2R}\left(1 - \frac{y_0}{R}\right) \geq 0$$

while

$$q(0) = -\frac{V}{2\pi C} < 0.$$

Therefore, for the existence of a single root $0 \leq y_0 \leq R$ of Equation 31, it is necessary and sufficient that

$$q(R) = \frac{R^3}{40} - \frac{V}{2\pi C} \geq 0,$$

or equivalently

$$V \leq \frac{C\pi R^3}{20}.$$

Define

$$V_c = \frac{C\pi R^3}{20} = \left(\frac{30\tau_M}{\rho_0 f k}\right)^{\frac{1}{2}} \frac{\pi R^3}{20}. \tag{32}$$

Then V_c represents the "critical volume" such that if $V < V_c$, then the isopycnal will outcrop; if $V > V_c$, then the isopycnal will not outcrop. If $V = V_c$, then outcropping will occur at $y_0 = R$. A contour plot of V_c as a function of the wind stress τ_M and eddy efficiency k is given in Figure 6.

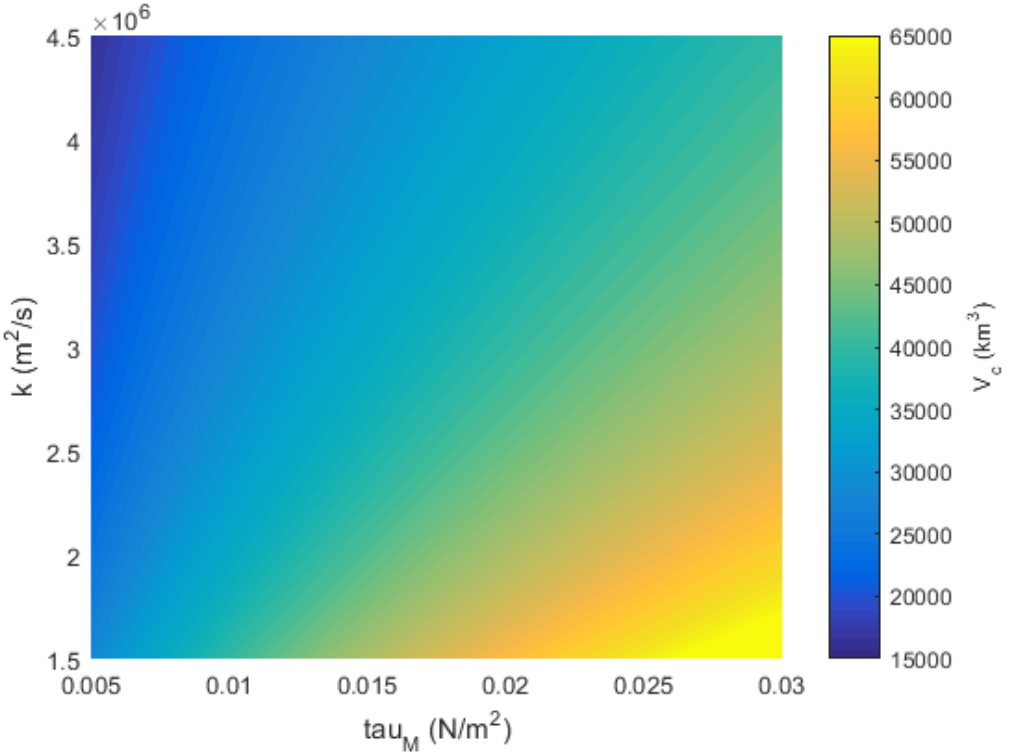

Figure 6: Plot of the critical volume V_c defined in Equation 32 as a function of the mean surface wind stress τ_M and the eddy efficiency k. Reference values for the model are $\tau_M = 0.015$ N m^{-2} and $k = 3 \cdot 10^6$ m^2 s^{-1}.

2.5 Numerical solution of the nonlinear problem

Consider the nonlinear problem

$$h_t = \frac{1}{r}(rKh_r)_r + \frac{1}{r}\left(r\frac{-\tau}{\rho_0 f}\right)_r \tag{33}$$

with

$$K = ks = k|h_r| \tag{34}$$

and

$$h_r|_{r=0,R} = 0. \tag{35}$$

We assume that τ is a known function given by Equation 20. As previously noted, we wish to relax the assumption of a fixed isopycnal depth at the gyre boundary in [7]. Using these boundary conditions and the choice of τ according to Equation 20 (specifically, $\tau(0) = \tau(R) = 0$), it follows from Equation 33 that

$$V_t = 2\pi \int_0^R r h_t \, dr = 0$$

i.e., the gyre volume is conserved. However, if $h(r,t)$ changes sign on $0 \leq r \leq R$, then the positive volume bounded between the isopycnal and the surface is not conserved. In addition, a constraint is needed to prevent $h < 0$, which is physically unrealistic. Thus, a modification of Equation 33 is needed and we introduce a regularization factor F given by

$$F(h) = 100 \exp(-10h) + 1. \tag{36}$$

The modified halocline depth evolution equation is given by

$$h_t = \frac{1}{r}(rKFh_r)_r + \frac{1}{r}\left(r\frac{-\tau}{\rho_0 f}\right)_r. \tag{37}$$

Now if $h \leq 0$, then $F(h)$ is very large, i.e., the diffusion term is strong. However, if $h \geq 0$, then $F(h) \approx 1$, so that $F(h)$ does not modify the solution. An added benefit is that if $h \geq 0$ for all r and t, then the positive volume bounded between the isopycnal and the surface will be conserved.

We implement a numerical scheme using the "pdepe" package in Matlab to solve Equation 37 to steady state ($\sim$3 years) for three initial volumes ($0.5V_c$, V_c, and $1.5V_c$). The results are compared in Figure 7 with the theoretical steady state solution given by Equation 26 and reveal that the model closely approaches the theoretical steady state with minimal volume "loss" (i.e., negative signed volume).

In addition, we explore the steady state solution as a function of the wind stress and initial volume of the gyre (Figures 8 and 9). Strong mean surface wind stress deepens the halocline near the gyre interior and shoals it near the boundary (Figure 8). Figure 9 shows the steady state solution for the critical volume with $\tau_M = 0.015$ N m^{-2} (yellow curve) and for various fractions of the critical volume. For $\tau_M = 0.015$ N m^{-2}, it turns out that $V_c \approx 34,600$ km^3.

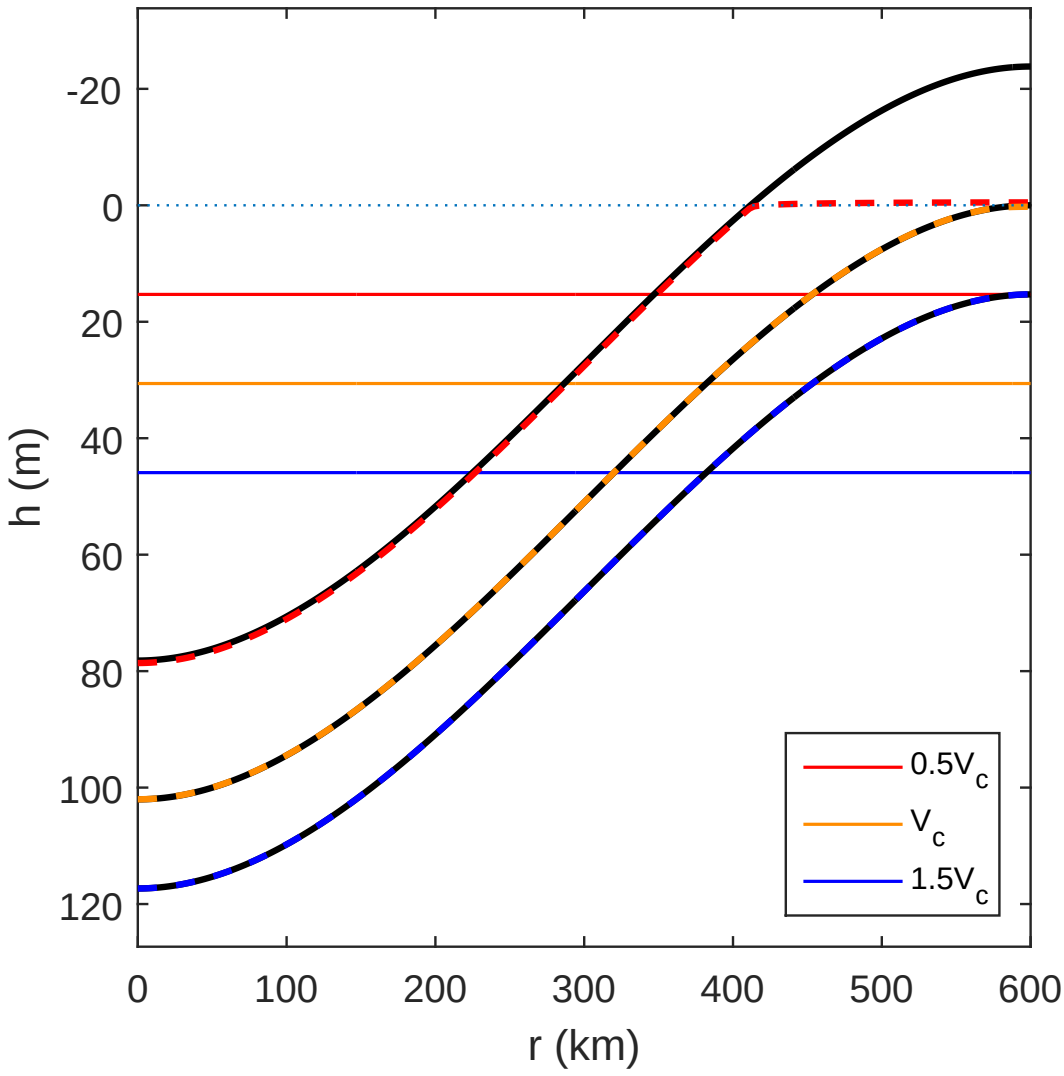

Figure 7: Initial (flat colored lines) and steady state (dashed colored lines) h as obtained from Equation 37 with initial conditions chosen such that the initial volumes are $0.5V_c, V_c$, and $1.5V_c$; theoretical solution of Equation 26 for corresponding volumes (black curves).

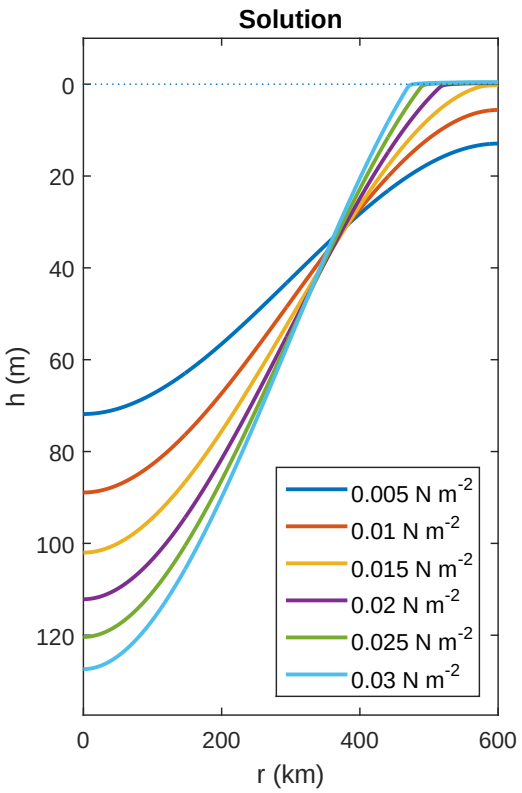

Figure 8: Steady state solutions of Equation 37 for varying choices of τ_M. Each equation is initialized from a constant state $h_0(r) = V_c/\pi R^2$, where V_c is the critical volume for $\tau_M = 0.015$ N m^{-2}. (Thus, V_c is the volume bounded between the yellow curve and the surface.)

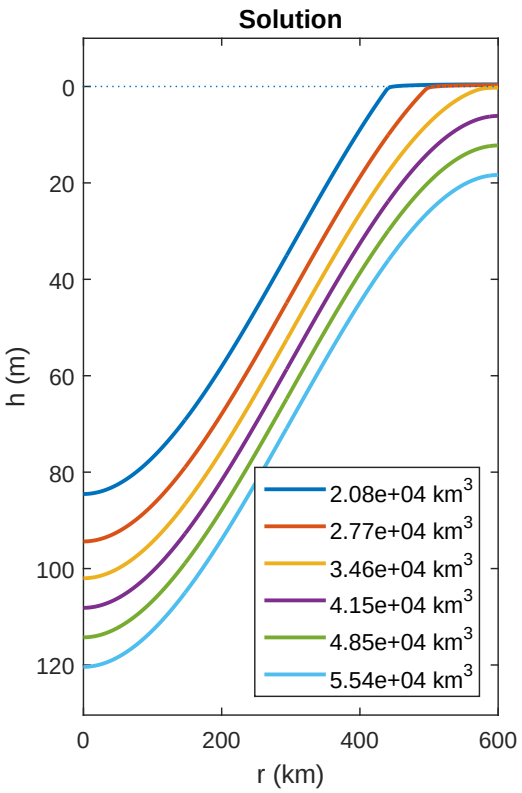

Figure 9: Steady state solutions of Equation 37 for varying initial volume V. Each equation is initialized from a constant state $h_0(r) = V/\pi R^2$. The yellow curve shows the solution for the critical volume V_c with $\tau_M = 0.015$ N m^{-2}.

3 Multi-layer Model

Integrating Equation 33 with $h_t = 0$ reveals that in steady state,

$$h_r = \frac{\tau}{\rho_0 f K} \tag{38}$$

or with the assumption $K = k|h_r|$,

$$h_r = -\left(-\frac{\tau}{\rho_0 f k}\right)^{\frac{1}{2}}.$$

In any case, in steady state, the slope h_r is directly proportional to the surface wind stress and inversely proportional to the eddy diffusivity/eddy efficiency. However, Figure 3 reveals considerable vertical variation of the winter and summer mean halocline slope. Specifically, between about ∼50-200 m, the isopycnal slope rapidly increases with depth. Evidently, the single-layer halocline model cannot capture this vertical variation.

In addition, estimates of the along-isopycnal eddy diffusivity have recently been derived from observations at four moorings in the Beaufort Gyre using the scaling law

$$K \sim (EKE)^{\frac{1}{2}} \cdot l$$

where EKE represents the eddy kinetic energy and l represents a mixing length scale [8]. Figure 11 reveals that the eddy diffusivity decreases with depth, which is not immediately consistent with the parameterization of the eddy diffusivity K as directly proportional to the isopycnal slope h_r.

3.1 Multi-layer uncoupled model with observed eddy diffusivity

In order to attempt to capture the observed vertical variation of the halocline slope, we consider a multi-layer model in which each isopycnal has a depth evolution equation given by

$$h_{it} = \frac{1}{r}(rFK_i h_{ir})_r + \frac{1}{r}\left(r\frac{-\tau}{\rho_0 f}\right)_r \tag{39}$$

for $1 \leq i \leq N$, where N represents the number of interfaces. The boundary conditions for each interface are given by Equation 35 and the surface wind stress τ is given by Equation 20. Here K_i is a constant with respect to r and t. Note that in this model, the isopycnal depths evolve independently of each other (i.e., the interfaces are uncoupled).

As for the nonlinear single-layer halocline model, we solve Equation 39 numerically to steady state (∼10 years), initializing each equation from a state of constant depth z_i (Figure 10). Here K_i is estimated from the mean diffusivity observed in the Beaufort Gyre at a sequence of depths $z_i = \{30, 80, 130, 180, 230, 280\}$ m (see Figure 11, red line). Since the observed diffusivity is noisy, we fit a cubic interpolant to a series of points from the observed

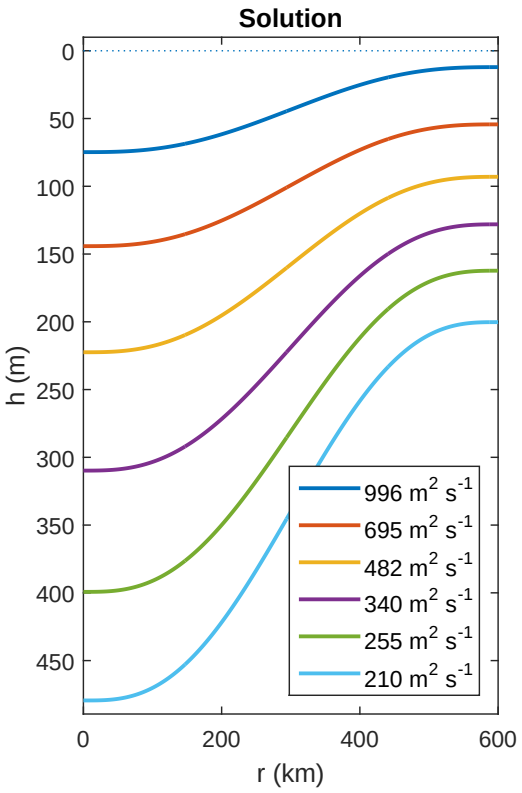

Figure 10: Steady state solutions of Equation 39 for each isopycnal interface with constant eddy diffusivity K_i indicated in the legend.

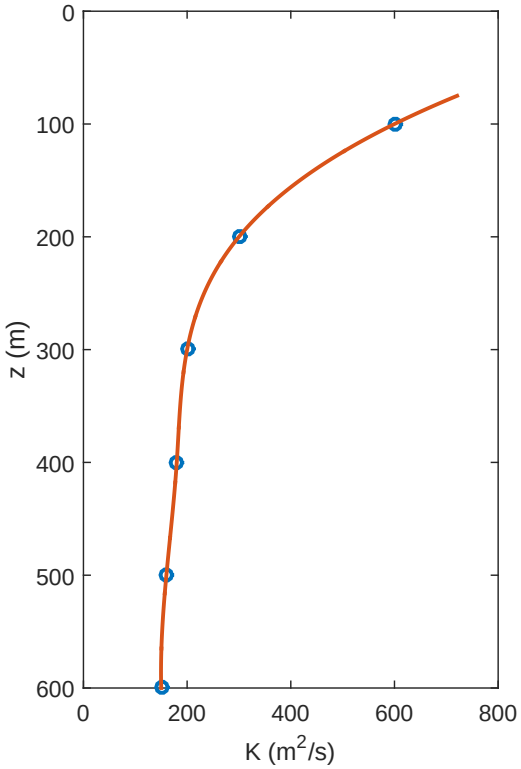

Figure 11: Vertical profile of the estimated along-isopycnal eddy diffusivity (K_λ) in the Beaufort Gyre. Estimates from mean of four moorings in [8] (blue circles) and interpolated profile (red curve).

data and use it to estimate K_i for each depth z_i. The applied diffusivities and steady state layer depths are shown in Figure 10.

Thus, this simple model is able to capture the observed mean vertical structure of the halocline, and in particular, the increase of isopycnal slope with depth beneath the mixed layer (Figure 3, right column). However, the model does not explain what processes determine the observed vertical profile of the eddy diffusivity in the first place.

3.2 Multi-layer coupled model

By Equation 38, which was derived in the absence of boundary fluxes, it follows that a necessary condition for vertical variation of the isopycnal slope is vertical variation of the eddy diffusivity. Specifically, in steady state the ratio of the interface slopes satisfies

$$\frac{H_{1r}}{H_{2r}} = \frac{K_2}{K_1}.$$

(From now on, h will denote a layer thickness and H will denote the depth of a particular isopycnal interface, a distinction that will become relevant in the following derivation.)

A multi-layer coupled model should be capable of capturing the observed variation of the halocline slope and eddy diffusivity with depth. As has been demonstrated, the existing model with a given interface-dependent eddy diffusivity can capture the observed halocline slope in steady state. However, it cannot explain how the gyre equilibrated to the observed state with the observed vertical variation of eddy diffusivity. Baroclinic instability, and thus the eddy diffusivity at any point in time, should depend not only upon the local interface slope H_{ir}, but upon the stability characteristics of the entire water column. Therefore, we construct a multi-layer coupled model in which each interface depth H_i evolves according to

$$H_{it} = \frac{1}{r}\left(rFK_iH_{ir}\right)_r + \frac{1}{r}\left(r\frac{-\tau}{\rho_0 f}\right)_r \tag{40}$$

for $i = \{1, 2\}$. This equation is accompanied by the boundary condition

$$H_{ir}|_{r=0,R} = 0, \tag{41}$$

i.e., there is no flux of height (equivalently, volume) through the boundary. We consider a three-layer model, which represents a compromise between the need to accurately capture instability that arises from interactions between layers and the desire for simplicity and to keep computational demands low.

Equation 40 is solved through the iterative process illustrated in Figure 12. First, the time interval $t_0, \ldots t_N$ on which the solution is desired is subdivided into a number of equally-spaced segments $t_j, \ldots, t_{j+M}$. Beginning at time t_0, the initial layer slopes and densities are used to calculate the geostrophic velocities in the θ-direction in each layer from the multi-layer shallow water equations. The resulting profile of the water column can be baroclinically unstable, i.e., the tilt of the isopycnals relative to the isobars can represent a

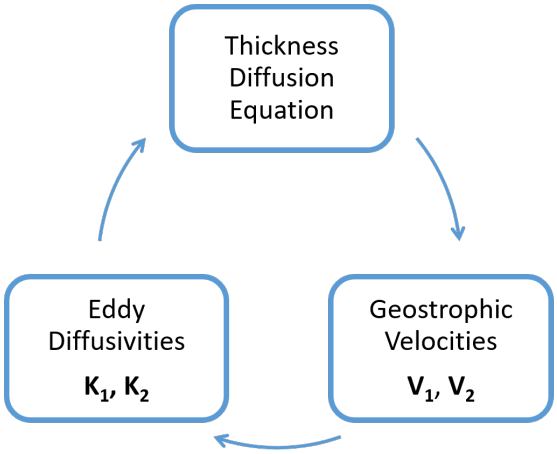

Figure 12: Process model of the solution method of the three-layer coupled model.

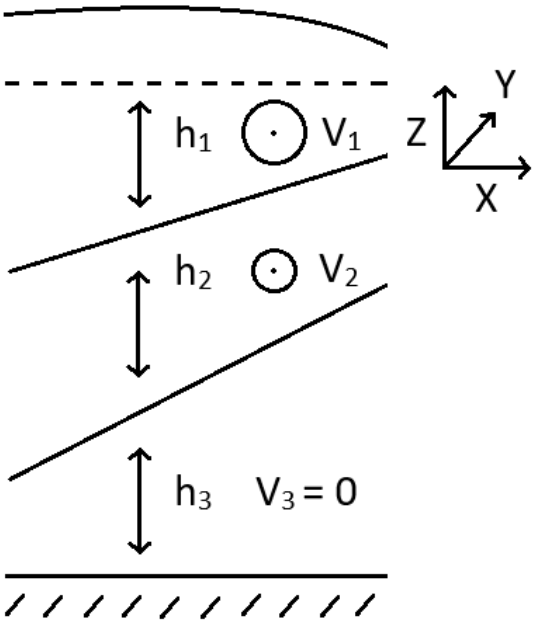

Figure 13: Schematic diagram of the layer thicknesses h_i and layer geostrophic velocities V_i in the three-layer model.

source of potential energy that is converted into kinetic energy as the baroclinic instability (eddy) grows. Therefore, a stability analysis is performed in the setting of the multi-layer shallow water quasi-geostrophic potential vorticity equations and the eddy diffusivity K_i for each layer interface is estimated. Crucially, the eddy diffusivity depends upon the vertical profile of the isopycnal slope and geostrophic current such that Equation 40 represents a multi-layer coupled model in which the interfaces interact through the depth-varying eddy diffusivity K_i. The eddy diffusivities K_i are then used to integrate Equation 40 forward to time t_M, and the process of obtaining the geostrophic velocities and eddy diffusivities is repeated for the next segment beginning with the model state at time t_M. Equation 40 is thus integrated forward until the solution is obtained on the entire interval $t_0, \ldots t_N$. Due to the computational demands of this algorithm, we currently calculate K_i at a single spatial location and update the eddy diffusivity every M timesteps. More detailed derivations of these calculations follow.

3.2.1 Geostrophic velocities

The geostrophic velocities are obtained from the interface slopes and densities in the setting of the multi-layer shallow water approximation via the geostrophic relations. Using the hydrostatic relation and the simplified geometry in Figure 13, it follows that the pressure P_i in the ith layer is given by

$$
\begin{aligned}
P_1 &= \rho_1 g(\eta - z) \\
P_2 &= \rho_1 g\eta + \rho_1 g h_1 - \rho_2 g(z + h_1) \\
P_3 &= \rho_1 g\eta + \rho_1 g h_1 + \rho_2 g h_2 - \rho_3 g(z + h_1 + h_2),
\end{aligned}
$$

where η represents the sea surface height perturbation. Differentiating with respect to r yields

$$
\begin{aligned}
\frac{\partial P_1}{\partial r} &= \rho_1 g \frac{\partial \eta}{\partial r} \\
\frac{\partial P_2}{\partial r} &= (\rho_2 - \rho_1) g \frac{\partial h_1}{\partial r} + \rho_1 g \frac{\partial \eta}{\partial r} \\
\frac{\partial P_3}{\partial r} &= (\rho_3 - \rho_1) g \frac{\partial h_1}{\partial r} + (\rho_3 - \rho_2) g \frac{\partial h_2}{\partial r} + \rho_1 g \frac{\partial \eta}{\partial r}.
\end{aligned}
$$

The system can be closed by imposing $V_3 = 0$, i.e., the assumption of no motion in the deep bottom layer. This then implies that

$$
\begin{aligned}
V_1 &= \frac{g}{\rho_0 f}\left[(\rho_3 - \rho_1)\frac{\partial h_1}{\partial r} + (\rho_3 - \rho_2)\frac{\partial h_2}{\partial r}\right] \\
V_2 &= \frac{g}{\rho_0 f}\left[(\rho_3 - \rho_2)\frac{\partial h_1}{\partial r} + (\rho_3 - \rho_2)\frac{\partial h_2}{\partial r}\right].
\end{aligned}
$$

Now letting $\rho_0 = \rho_1$ and defining the reduced gravity g_i' as

$$
g_i' = \frac{\rho_{i+1} - \rho_i}{\rho_1} g \tag{42}
$$

it follows that

$$
\begin{aligned}
V_1 &= \frac{1}{f}\left[(g_2' + g_1')\frac{\partial h_1}{\partial r} + g_2'\frac{\partial h_2}{\partial r}\right] \\
V_2 &= \frac{1}{f}\left[g_2'\frac{\partial h_1}{\partial r} + g_2'\frac{\partial h_2}{\partial r}\right].
\end{aligned} \tag{43}
$$

3.3 Stability analysis

The following theory is developed in [11]. Given the geostrophic velocities, we perform a stability analysis on the linearized multi-layer shallow water quasi-geostrophic potential vorticity equations. Given the shallow water approximation, in each layer the potential vorticity Q_i satisfies

$$
\frac{DQ_i}{Dt} = 0, \quad Q_i = \frac{\zeta_i + f}{h_i}
$$

where ζ_i is the relative vorticity of the fluid, f is the planetary vorticity, and h_i is the layer thickness. In other words, the potential vorticity is a conserved quantity. Assuming that 1) variations in layer thickness are small relative to the total layer thickness; 2) the Rossby number is small; and 3) variations in the Coriolis parameter are small, then this equation can be linearized to give the so-called quasi-geostrophic potential vorticity in each layer,

$$q_i = \left(\beta y + \zeta_i - f_0 \frac{h_i'}{H_i} \right),$$

which is also conserved. Here H_i represents the basic state layer thickness and h_i' represents a layer thickness perturbation. For simplicity, we assume that $\beta = 0$.

The N-layer multi-layer shallow water equations may be obtained by introducing a streamfunction ψ_i for each layer. Then the potential vorticity q_i in each layer $1 \leq i \leq N$ can be expressed as

$$q_1 = \nabla^2 \psi_1 + \frac{f_0^2}{H_1} \left(\frac{\psi_2 - \psi_1}{g_1'} - \frac{f_0^2}{g H_1} \psi_1 \right) \tag{44}$$

$$q_i = \nabla^2 \psi_i + \frac{f_0^2}{H_i} \left(\frac{\psi_{i-1} - \psi_i}{g_{i-1}'} - \frac{\psi_i - \psi_{i+1}}{g_i'} \right) \tag{45}$$

$$q_N = \nabla^2 \psi_N + \frac{f_0^2}{H_N} \left(\frac{\psi_{N-1} - \psi_N}{g_{N-1}'} + \frac{f_0}{H_n} \eta_b \right), \tag{46}$$

and evolves according to

$$\frac{\partial q_i}{\partial t} + J(\psi_i, q_i) = 0. \tag{47}$$

Here we assume that the bottom topography $\eta_b = 0$. We now investigate this system for the presence of baroclinic instability by linearizing Equations 44-46 and 47 (with $N = 3$) about a basic state layer potential vorticity Q_i, velocity V_i and streamfunction Ψ_i. Here V_i is constant in each layer and represents the velocity in the y-direction (see Figure 13). Then Equations 44-46 reduce to

$$\begin{bmatrix} q_1' \\ q_2' \\ q_3' \end{bmatrix} = \begin{bmatrix} \nabla^2 \psi_1' \\ \nabla^2 \psi_2' \\ \nabla^2 \psi_3' \end{bmatrix} + f_0^2 \begin{bmatrix} -\frac{1}{gH_1} - \frac{1}{g_1' H_1} & \frac{1}{g_1' H_1} & 0 \\ \frac{1}{g_1' H_2} & -\frac{1}{g_1' H_2} - \frac{1}{g_2' H_2} & \frac{1}{g_2' H_2} \\ 0 & \frac{1}{g_2' H_3} & -\frac{1}{g_2' H_3} \end{bmatrix} \begin{bmatrix} \psi_1' \\ \psi_2' \\ \psi_3' \end{bmatrix} \tag{48}$$

Separating the terms in Equation 47 into sums of basic state variable and perturbations (indicated by primes) yields

$$\begin{aligned} &\frac{\partial q_i'}{\partial t} + \frac{\partial Q_i}{\partial t} + \frac{\partial \psi_i'}{\partial x}\frac{\partial q_i'}{\partial y} + \frac{\partial \psi_i'}{\partial x}\frac{\partial Q_i}{\partial y} + \frac{\partial \Psi_i}{\partial x}\frac{\partial q_i'}{\partial y} + \frac{\partial \Psi_i}{\partial x}\frac{\partial Q_i}{\partial y} \\ &\qquad - \frac{\partial \psi_i'}{\partial y}\frac{\partial Q_i}{\partial x} - \frac{\partial \psi_i'}{\partial y}\frac{\partial q_i'}{\partial x} - \frac{\partial \Psi_i}{\partial y}\frac{\partial Q_i}{\partial x} - \frac{\partial \Psi_i}{\partial y}\frac{\partial q_i'}{\partial x} = 0. \end{aligned}$$

Subtracting the equation satisfied by the basic state variables and assuming that products of perturbations are small, the linearized potential vorticity evolution equation reduces to

$$\frac{\partial q_i'}{\partial t} + \frac{\partial \psi_i'}{\partial x}\frac{\partial Q_i}{\partial y} + \frac{\partial \Psi_i}{\partial x}\frac{\partial q_i'}{\partial y} - \frac{\partial \psi_i'}{\partial y}\frac{\partial Q_i}{\partial x} - \frac{\partial \Psi_i}{\partial y}\frac{\partial q_i'}{\partial x} = 0.$$

Now by assumption, there are no gradients of basic state variables in the y-direction, so this equation further reduces to

$$\frac{\partial q_i'}{\partial t} + V_i\frac{\partial q_i'}{\partial y} + u_i'\frac{\partial Q_i}{\partial x} = 0 \tag{49}$$

after making use of the streamfunction relations. Here

$$\begin{bmatrix} \frac{\partial Q_1}{\partial x} \\ \frac{\partial Q_2}{\partial x} \\ \frac{\partial Q_3}{\partial x} \end{bmatrix} = f_0^2 \begin{bmatrix} -\frac{1}{gH_1} - \frac{1}{g_1'H_1} & \frac{1}{g_1'H_1} & 0 \\ \frac{1}{g_1'H_2} & -\frac{1}{g_1'H_2} - \frac{1}{g_2'H_2} & \frac{1}{g_2'H_2} \\ 0 & \frac{1}{g_2'H_3} & -\frac{1}{g_2'H_3} \end{bmatrix} \begin{bmatrix} V_1 \\ V_2 \\ V_3 \end{bmatrix}. \tag{50}$$

Now define

$$L_z := f_0^2 \begin{bmatrix} -\frac{1}{gH_1} - \frac{1}{g_1'H_1} & \frac{1}{g_1'H_1} & 0 \\ \frac{1}{g_1'H_2} & -\frac{1}{g_1'H_2} - \frac{1}{g_2'H_2} & \frac{1}{g_2'H_2} \\ 0 & \frac{1}{g_2'H_3} & -\frac{1}{g_2'H_3} \end{bmatrix}.$$

We search for potential vorticity perturbations with a wave-like structure in the y-direction that are growing in time. Specifically, assuming the ansatz

$$q_i' = \Re\left[\tilde{q}_i e^{ik(y-ct)}\right], \qquad {}_i' = \Re\left[\tilde{\psi}_i e^{ik(y-ct)}\right], \tag{51}$$

and substituting Equations 50 and 51 into Equation 49 yields

$$V_i\tilde{q}_i - \tilde{\psi}_i\frac{\partial Q_i}{\partial x} = c\tilde{q}_i, \tag{52}$$

where, by Equation 48,

$$\tilde{q}_i = (L_z - k^2 I)\tilde{\psi}_i.$$

Therefore, Equation 52 is equivalent to a matrix eigenvalue problem that can be solved numerically for c and $\tilde{q}_i$. For every wavenumber k, there are three eigenvalues c_1, c_2, c_3 and corresponding eigenvectors $\tilde{q_{i1}}, \tilde{q_{i2}}, \tilde{q_{i3}}$ that solve the system. By Equation 51, the fastest-growing perturbation is represented by the eigenvector whose corresponding eigenvalue has

maximum imaginary part. Therefore, we search numerically over a range of wavenumbers spanning the baroclinic deformation radii for the maximum baroclinic instability growth rate given by

$$\lambda = \max_k k\Im[c], \tag{53}$$

and therefore

$$\begin{aligned} q_i' &= e^{\lambda t}(\Re[\tilde{q_i}]\cos(ky) + i\Im[\tilde{q_i}]\sin(ky)) \\ u_i' &= e^{\lambda t}(\Re[\tilde{u_i}]\cos(ky) + i\Im[\tilde{u_i}]\sin(ky)) \end{aligned}$$

and

$$\begin{aligned} q_i'u_i' = e^{2\lambda t}(&\Re[\tilde{q_i}]\Re[\tilde{u_i}]\cos^2(ky) + \Im[\tilde{q_i}]\Im[\tilde{u_i}]\sin^2(ky) \\ &- \Re[\tilde{q_i}]\Im[\tilde{u_i}]\sin(ky)\cos(ky) - \Im[\tilde{q_i}]\Re[\tilde{u_i}]\sin(ky)\cos(ky)). \end{aligned}$$

Averaging meridionally,

$$\overline{q_i'u_i'} \sim (\Re[\tilde{q_i}]\Re[\tilde{u_i}] + \Im[\tilde{q_i}]\Im[\tilde{u_i}]).$$

Now the layer eddy diffusivity κ_i that we seek is given by

$$\kappa_i = -\frac{\overline{q_i'u_i'}}{Q_{ix}}. \tag{54}$$

However, $\overline{q_i'u_i'}$ is known only up to a constant factor. Therefore, we choose the parameterization

$$\hat{\kappa_i} = -\frac{\Re[\tilde{q_i}]\Re[\tilde{u_i}] + \Im[\tilde{q_i}]\Im[\tilde{u_i}]}{Q_{ix}}, \quad \kappa_i = k_c\lambda\frac{\hat{\kappa_i}}{\max_i \hat{\kappa_i}}$$

where $k_c = 10^9$ is chosen such that k_i has the observed order of magnitude for eddy diffusivity in the Beaufort Gyre halocline (i.e., 100-1000 $\mathrm{m}^2\ \mathrm{s}^{-1}$). Thus, κ_i is proportional to the baroclinic instability growth rate λ and comparing $\hat{\kappa_i}/\hat{\kappa_j}$ for $i \neq j$ reflects the ratio of the eddy diffusivities between the layers.

Notably, κ_i represents the eddy diffusivity of the i-th layer, rather than the i-th interface. However, the geometry of the three-layer model (Figure 13) suggests that $K_1 = \kappa_1$ and $K_2 = \kappa_3$, where K_i represents the eddy diffusivity coefficient for the i-th interface.

3.4 Results

Using this algorithm, we investigate the solution of Equation 40 in steady state. Specifically, we initialize the model from numerous configurations of initial isopycnal slopes (Figure 15, red dots) and integrate forward until the model reaches steady state (typically ∼5 years). In all cases, the model evolves to a steady state in which the isopycnals are approximately parallel (Figure 15, black dots), i.e., $S_1 \approx S_2$ and $K_1 \approx K_2$. Figure 14 illustrates the evolution to steady state for a representative case.

Figure 15 reveals that there are two configurations for the vertical profile of the eddy diffusivity; these configurations correspond to the two baroclinic modes in the three-layer problem (Figure 16). A sign change of the basic state potential vorticity gradient between layers is a necessary condition for baroclinic instability. If this sign change occurs between the second and third layers, then the baroclinic instability can be dominated by the first baroclinic mode and $K_1 \approx K_2$. On the other hand, if the sign change occurs between the first and second layers, then the instability can be dominated by the second baroclinic mode and $K_2 << K_1$.

Regardless of the initial conditions, the model evolves to a steady state in which $S_1 \approx S_2$, i.e., the line $S_1 = S_2$ is an attractor (Figure 15). The magnitude of the final slopes is determined by the wind stress τ.

However, the observed winter and summer mean isopycnal slopes in the Beaufort Gyre are depth-dependent (Figure 3, right column). In order to obtain depth-dependent isopycnal slopes in steady state, it is necessary to introduce fluxes of potential vorticity (equivalently, volume) at the gyre boundary. The following is a simplified proof-of-concept that is solved analytically.

Suppose that a flux of volume Q enters the second layer only, and that no flux enters the first layer, through the gyre boundary. Specifically, the boundary conditions for the second layer thickness are

$$h_{2r}|_{r=0} = 0, \quad Kh_{2r}|_{r=R} = \frac{Q}{2\pi R}.$$

In order to preserve the gyre volume, it is necessary to remove an equivalent volume from the gyre interior, distributed across the entire gyre. Specifically, the thickness evolution equation is given by

$$h_{2t} = \frac{1}{r}\left(rKh_{2r}\right)_r - \frac{Q}{\pi R^2}.$$

(Here we are assuming that $K = K_1 = K_2$.) This equation satisfies

$$2\pi \int_0^R r h_{2t} = 0,$$

i.e., the volume bounded between the first and second interfaces is constant with respect to time. The steady-state solution of this equation is given by

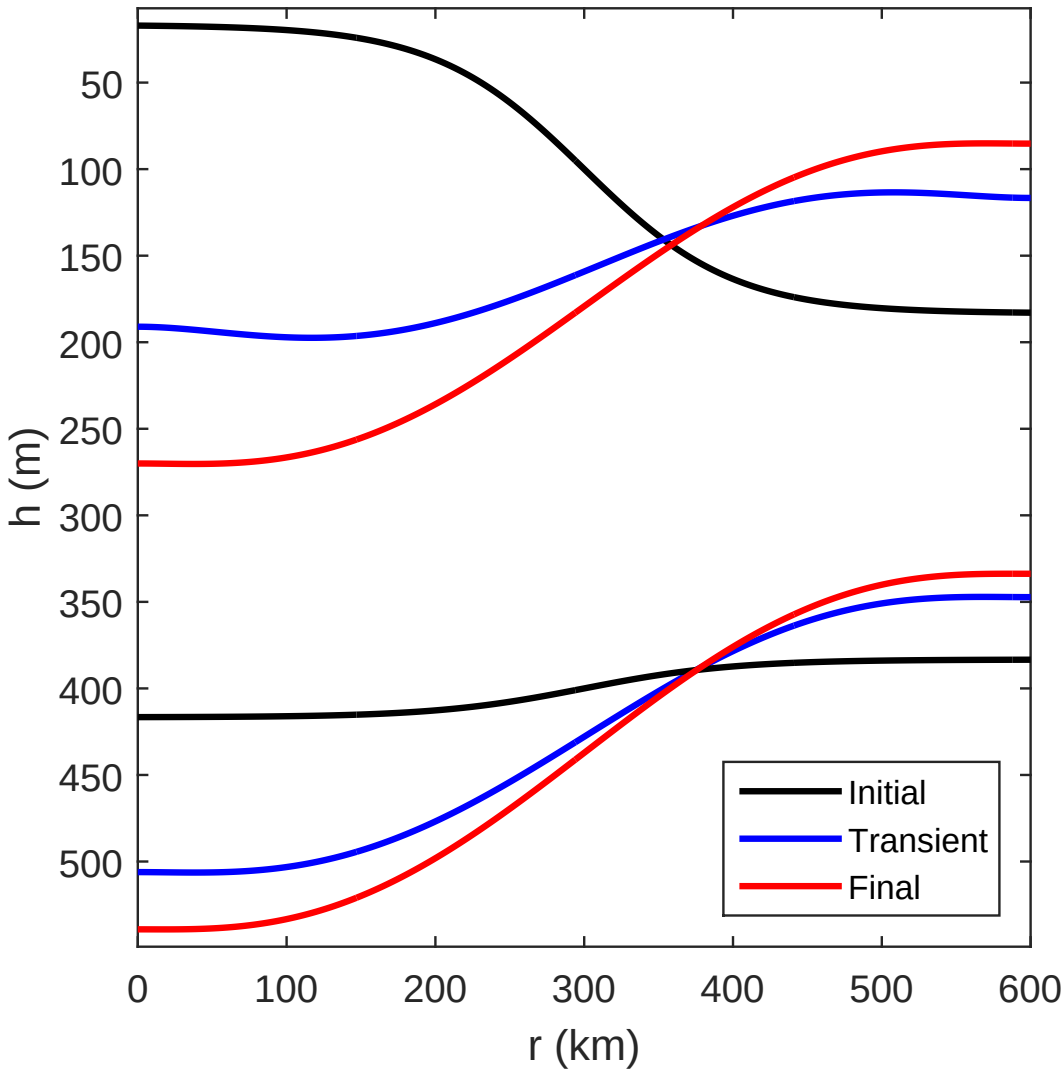

Figure 14: Example of the evolution of the halocline depth in the multi-layer model to steady state (red curves; ∼5 years) from the indicated initial state (black curves). The model state after ∼2.5 years is also indicated (blue curves).

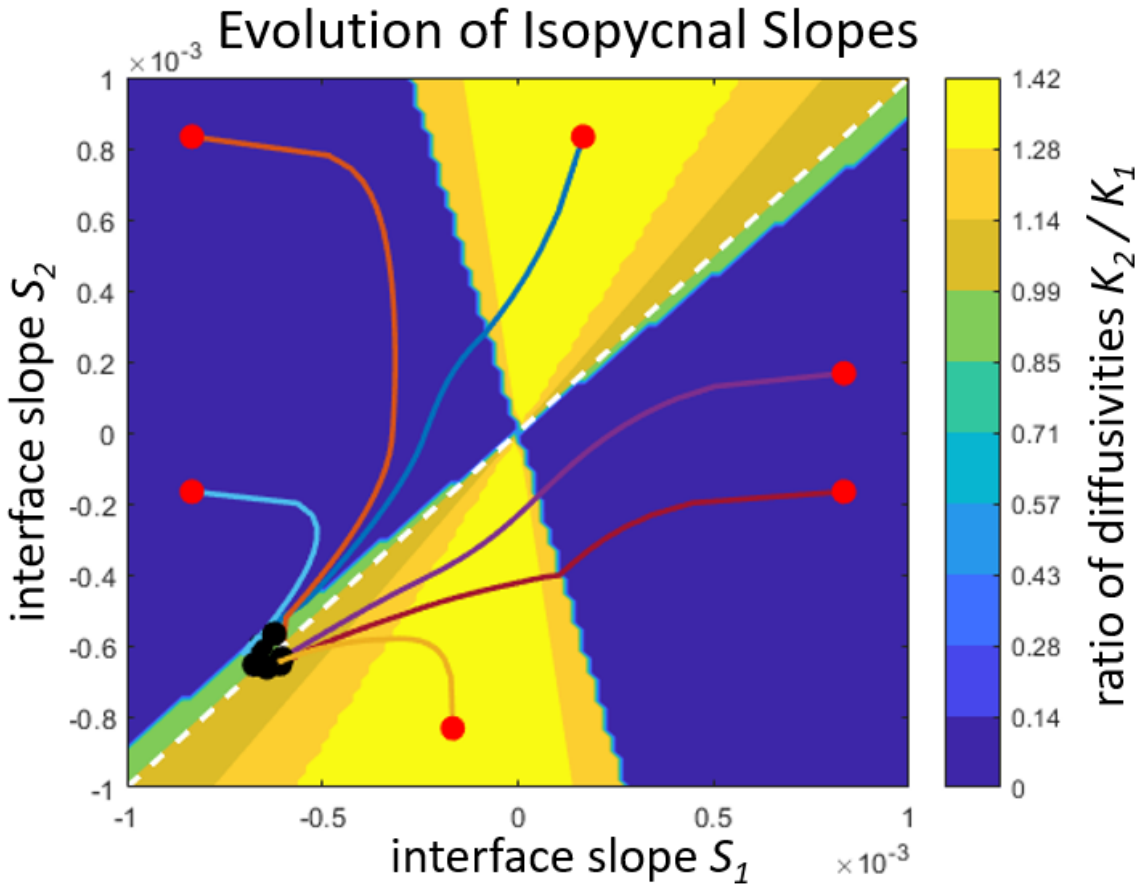

Figure 15: Ratio of diffusivities K_2 and K_1 as a function of the isopycnal slopes S_1 and S_2 (colormap). Slope trajectories from the three-layer coupled model (colored lines) for various choices of the initial slopes (red dots), and resulting steady-state slopes (black dots). The gyre attracts to a steady state of parallel slopes (i.e., $S_1 = S_2$; dashed white line). The wind stress τ_M determines the magnitude of the final slopes.

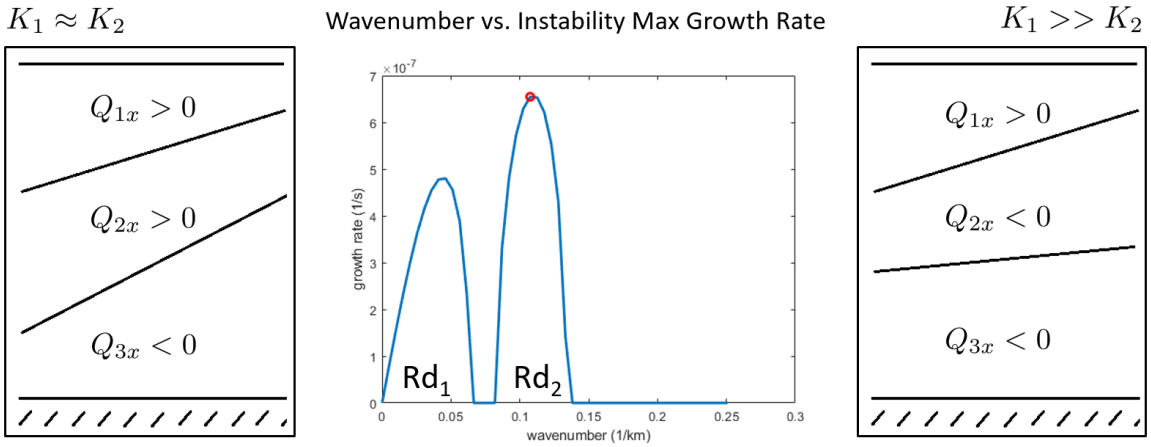

Figure 16: (Center) Example of maximum growth rate kc for various wavenumbers k and wavenumber corresponding to the maximum growth rate (red circle). In this case the instability is dominated by the second baroclinic mode. Sign change of PV gradient Q_{ix} is a necessary condition for baroclinic instability. (Left) Schematic diagram of water column profile and eddy diffusivities when the instability is dominated by the first baroclinic mode. (Right) Schematic diagram of water column profile and eddy diffusivities when the instability is dominated by the second baroclinic mode.

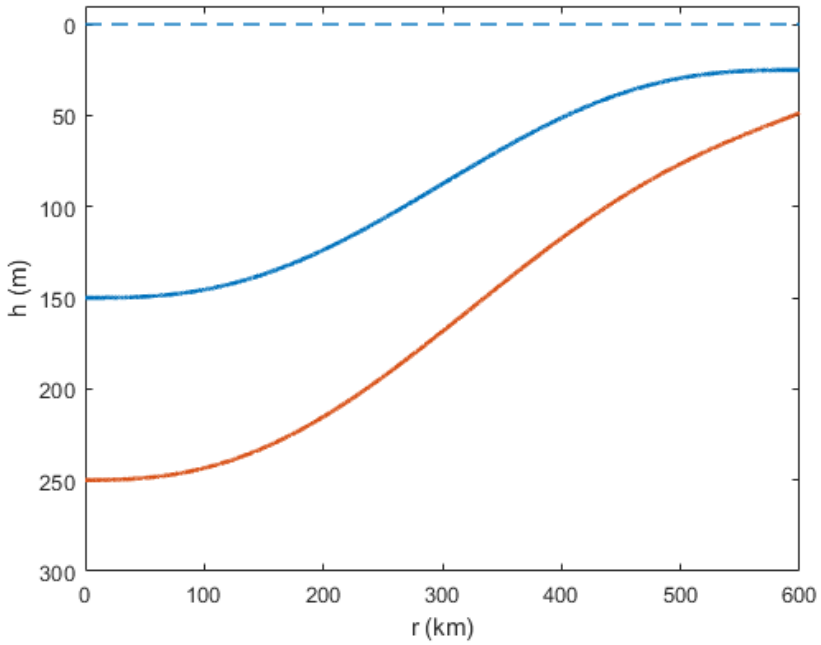

Figure 17: Solution of Equations 55 and 56 with $h_1(0) = 150$ m, $h_2(0) = 100$ m, and $Q = -15,000$ km^3 yr^{-1}.

$$h_2(r) = h_2(0) + \frac{Qr^2}{4\pi R^2 K}. \tag{55}$$

As before, the evolution equation for the first layer depth is given by

$$h_{1t} = \frac{1}{r}\left(rKh_{1r}\right)_r + \frac{1}{r}\left(r\frac{-\tau}{\rho_0 f}\right)_r$$

with boundary conditions

$$h_{1r}|_{r=0,R} = 0.$$

In steady state, the solution of this equation is given by

$$h_1(r) = h_1(0) - \frac{30\tau_M}{\rho_0 f K}\left(\frac{r^3}{3R^2} - \frac{r^4}{2R^3} + \frac{r^5}{5R^4}\right). \tag{56}$$

The solution of Equations 55 and 56 is shown in Figure 17 with some representative choices of the unspecified parameters ($h_1(0) = 150$ m, $h_2(0) = 100$ m, $Q = -15,000$ km^3 yr^{-1}. Here the boundary flux is exaggerated to show effect.) It can be seen that the isopycnal slope increases with depth.

4 Conclusions

Current adiabatic models of the Beaufort Gyre halocline represent it as a buoyant interface with a depth that is that is increased by Ekman pumping; the deepening is opposed by mesoscale eddy transport. In steady state, the isopycnal slope is predicted to be proportional to the strength of the surface wind stress and inversely proportional to the eddy diffusivity. Eddy diffusivity is often parameterized to be proportional to isopycnal slope, yet observations from the PHC climatology suggest that the isopycnal slope increases with depth, while mooring-derived along-isopycnal eddy diffusivity decreases with depth. This suggests that the current theory should be reconsidered.

First, we have improved the single-layer halocline model from [7]. Specifically, seasonal outcropping of isopycnals is observed in the Beaufort Gyre, a phenomenon that the modified single-layer model can now capture. In this setting, we have also derived an expression for a so-called "critical volume" V_c that depends upon the wind stress and eddy diffusivity. The volume of the gyre in relation to the critical volume determines whether the halocline outcrops.

In addition, we have developed a multi-layer model in which the isopycnal interfaces are coupled with each other through the depth-dependent eddy diffusivity. The strength and vertical profile of the eddy diffusivity is determined from the baroclinic instability characteristics of the geostrophic currents, which are derived from the isopycnal slope via thermal wind balance. Using this simple model of eddy-mean flow interactions, we have identified

the critical processes that determine the vertical structure of the halocline. Specifically, we have shown that potential vorticity sources at the gyre boundary (over continental slopes) are key to setting up a realistic depth-varying distribution of the isopycnal slope in steady state. In the absence of the boundary fluxes, the gyre attracts to a steady state with depth-independent isopycnal slope, regardless of the initial conditions. These findings further justify the need for observational constraints on boundary fluxes and eddy diffusivity.

5 Acknowledgements

I am grateful to have taken part in the WHOI GFD program and particularly appreciate the mentorship of Renske Gelderloos and Georgy Manucharyan. I also thank the program directors, Claudia Cenedese and Mary-Louise Timmermans, as well as the numerous scientists with whom we had productive conversations about the project: Sam Pegler, Joe Pedlosky, Jack Whitehead, Mary-Louise Timmermans, Glenn Flierl and others.

References

[1] D. Andrews and M. E. McIntyre, *Planetary waves in horizontal and vertical shear: The generalized Eliassen-Palm relation and the mean zonal acceleration*, Journal of the Atmospheric Sciences, 33 (1976), pp. 2031–2048.

[2] P. R. Gent and J. C. Mcwilliams, *Isopycnal mixing in ocean circulation models*, Journal of Physical Oceanography, 20 (1990), pp. 150–155.

[3] K. A. Giles, S. W. Laxon, A. L. Ridout, D. J. Wingham, and S. Bacon, *Western arctic ocean freshwater storage increased by wind-driven spin-up of the Beaufort Gyre*, Nature Geoscience, 5 (2012), pp. 194–197.

[4] T. W. Haine, B. Curry, R. Gerdes, E. Hansen, M. Karcher, C. Lee, B. Rudels, G. Spreen, L. de Steur, K. D. Stewart, et al., *Arctic freshwater export: Status, mechanisms, and prospects*, Global and Planetary Change, 125 (2015), pp. 13–35.

[5] IOC, SCOR, and IAPSO, *The international thermodynamic equation of seawater — 2010: Calculation and use of thermodynamic properties.*, 2010. 196 pp., Intergovernmental Oceanographic Commission, Manuals and Guides No. 56, UNESCO (English).

[6] G. E. Manucharyan and M. A. Spall, *Wind-driven freshwater buildup and release in the Beaufort Gyre constrained by mesoscale eddies*, Geophysical Research Letters, 43 (2016), pp. 273–282.

[7] G. E. Manucharyan, M. A. Spall, and A. F. Thompson, *A theory of the wind-driven Beaufort Gyre variability*, Journal of Physical Oceanography, 46 (2016), pp. 3263–3278.

[8] G. Meneghello, J. Marshall, S. T. Cole, and M.-L. Timmermans, *Observational inferences of lateral eddy diffusivity in the halocline of the Beaufort Gyre.* (manuscript in review), 2017.

[9] A. Proshutinsky, R. Bourke, and F. McLaughlin, *The role of the Beaufort Gyre in Arctic climate variability: Seasonal to decadal climate scales*, Geophysical Research Letters, 29 (2002).

[10] M.-L. Timmermans, J. Marshall, A. Proshutinsky, and J. Scott, *Seasonally derived components of the Canada Basin halocline*, Geophysical Research Letters, 44 (2017), pp. 5008–5015.

[11] G. K. Vallis, *Atmospheric and oceanic fluid dynamics*, Cambridge University Press, 2017.

[12] M. Visbeck, J. Marshall, T. Haine, and M. Spall, *Specification of eddy transfer coefficients in coarse-resolution ocean circulation models*, Journal of Physical Oceanography, 27 (1997), pp. 381–402.